CityU Scholars

Cooperative deformation in high-entropy alloys at ultralow temperatures

Naeem, Muhammad; He, Haiyan; Zhang, Fan; Huang, Hailong; Harjo, Stefanus; Kawasaki, Takuro; Wang, Bing; Lan, Si; Wu, Zhenduo; Wang, Feng; Wu, Yuan; Lu, Zhaoping; Zhang, Zhongwu; Liu, Chain T.; Wang, Xun-Li

MATERIALS SCIENCE

Cooperative deformation in high-entropy alloys at ultralow temperatures

Muhammad Naeem[1], Haiyan He[1], Fan Zhang[2], Hailong Huang[2], Stefanus Harjo[3], Takuro Kawasaki[3], Bing Wang[1], Si Lan[1,4], Zhenduo Wu[1], Feng Wang[5], Yuan Wu[2], Zhaoping Lu[2], Zhongwu Zhang[6], Chain T. Liu[5,7], Xun-Li Wang[1,8]*

High-entropy alloys exhibit exceptional mechanical properties at cryogenic temperatures, due to the activation of twinning in addition to dislocation slip. The coexistence of multiple deformation pathways raises an important question regarding how individual deformation mechanisms compete or synergize during plastic deformation. Using in situ neutron diffraction, we demonstrate the interaction of a rich variety of deformation mechanisms in high-entropy alloys at 15 K, which began with dislocation slip, followed by stacking faults and twinning, before transitioning to inhomogeneous deformation by serrations. Quantitative analysis showed that the cooperation of these different deformation mechanisms led to extreme work hardening. The low stacking fault energy plus the stable face-centered cubic structure at ultralow temperatures, enabled by the high-entropy alloying, played a pivotal role bridging dislocation slip and serration. Insights from the in situ experiments point to the role of entropy in the design of structural materials with superior properties.

INTRODUCTION

Materials' mechanical behaviors under extreme conditions have been a subject of intensive research. At high temperatures, plastic deformation is dictated by atomic diffusion, which causes degradation of strength, elongation, phase transformation, and precipitation (1). At low temperatures, a ductile-to-brittle transition is expected because the atomic mobility vanishes, limiting plastic deformation through, e.g., movement of dislocations (2). However, in complex materials, other deformation mechanisms become competitive at low temperatures, providing alternative mechanisms to deform. High-entropy alloy (HEA) is a case in point.

HEAs, which consist of multi-principal elements, are an intriguing class of structural materials with excellent strength—ductility combination, high fracture toughness, resistance against corrosion and hydrogen embrittlement (3–9). They also have good stability against radiation damage, hence deemed potential materials for advanced reactor applications (10, 11). Refractory HEAs are promising candidates for high-temperature applications, e.g., for aero-engines, due to their thermal stability at elevated temperatures (3, 12, 13). Superconductivity has also been reported in Ta-Nb-Hf-Zr-Ti HEA, thus extending their possible applications beyond structural materials (14). Despite the complex chemistry, HEAs can form a single-phase solid solution with an incredibly simple lattice. For example, CrMnFeCoNi HEA, also known as Cantor alloy, has a face-centered cubic (fcc) structure (4, 6).

At room temperature, the deformation in the quinary CrMnFeCoNi and quaternary CrFeCoNi alloys is dominated by dislocation activities (4, 15, 16). At 1000 K, the major deformation mechanism is diffusion-controlled dislocation creep (17). At liquid-nitrogen temperature, CrMnFeCoNi shows both increased strength and ductility (4, 15). Although the activation of twinning, in addition to dislocation slip, is considered the main reason for the unusual ductility (4, 15), other mechanisms may also contribute, especially when the temperature is further lowered. In stainless steels, for example, martensitic transformation can occur, leading to the so-called TRIP (transformation-induced plasticity) effect (18). First-principle ab initio calculations by Huang et al. (19) suggested fcc to hcp (hexagonal close-packed) phase transformation in CrMnFeCoNi HEA below 77 K. At very low temperatures, such as liquid-helium temperature, serrated deformation has been observed, which usually deteriorates the ductility (20, 21). The different deformation mechanisms depend sensitively on the composition and microstructure. A key issue, in the presence of multiple deformation mechanisms, is at what stage each deformation mechanism emerges and how they contribute to the hardening behaviors. To this end, in situ observations are vitally important to determine the activation of different deformation mechanisms and understand their interactions during subsequent deformation. In particular, for deformation involving phase transformation, an in situ study at the test temperature is the only way to observe the influence of phase transformation on deformation.

Up to now, deformation behavior at ultralow temperatures, where a myriad of deformation mechanisms is expected, has remained a largely unexplored territory, and no in situ study has been reported. Conventional experimental methods, such as transmission electron microscope (TEM), cannot meet the demand, because in situ experiments are difficult to implement at extremely low temperatures. In addition, the field of view by TEM is limited (22). In situ neutron diffraction is a powerful technique to identify deformation mechanisms (23, 24). In particular, because neutrons are highly penetrating, the neutron diffraction measurements are representative of the bulk of the sample rather than from the surface or local areas. While this method has been routinely used at room temperature, recent

[1]Department of Physics, City University of Hong Kong, 83 Tat Chee Avenue, Kowloon, Hong Kong. [2]State Key Laboratory for Advanced Metals and Materials, University of Science and Technology Beijing, Beijing 100083, China. [3]J-PARC Center, Japan Atomic Energy Agency, Tokai, Ibaraki 319-1195, Japan. [4]Herbert Gleiter Institute of Nanoscience, Nanjing University of Science and Technology, Nanjing, Jiangsu 210094, China. [5]Department of Materials Science and Engineering, City University of Hong Kong, 83 Tat Chee Avenue, Kowloon, Hong Kong. [6]Institute for Metallic Materials, College of Materials Science and Chemical Engineering, Harbin Engineering University, Harbin 150001, China. [7]Department of Mechanical Engineering, City University of Hong Kong, 83 Tat Chee Avenue, Kowloon, Hong Kong. [8]City University of Hong Kong Shenzhen Research Institute, 8 Yuexing 1st Road, Shenzhen Hi-Tech Industrial Park, Shenzhen 518057, China.
*Corresponding author. Email: xlwang@cityu.edu.hk

advances have made low-temperature measurements possible (*25*). Here, in situ neutron diffraction measurements were conducted on three representative fcc HEAs, i.e., CrMnFeCoNi, CrFeCoNi, and CrCoNi, which all showed a multistage deformation process. The prototypic deformation behavior is illustrated with the data of CrMnFeCoNi HEA, unless otherwise noted. The aim of this study was to establish the deformation pathway for HEAs at ultralow temperatures and to elucidate the interaction and competition between different deformation mechanisms.

RESULTS

Crystal structure and load curves at 15 K

The neutron detector banks at ±90° provided diffraction data along the loading and transverse directions, designated as LD and TD, respectively. The CrMnFeCoNi HEA has a single-phase fcc crystal structure at room temperature, which remained stable on cooling to 15 K and during deformation at 15 K to failure. The change in the lattice parameter during cooling is depicted in fig. S1. The evolution of the selected diffraction patterns is shown in Fig. 1A. No additional peaks were found, either during cooling or deformation, indicating the structural stability down to 15 K. The complete structure evolution during cooling and loading is presented in fig. S2. During the deformation, pronounced texture development was observed in addition to a shift in peak positions. Notably, (220)//LD disappeared almost entirely toward the end of deformation. Furthermore, the diffraction peaks also show significant broadening at large deformations.

The true stress-strain curves are presented in Fig. 1B. On cooling, the strength and ductility both increased. At 15 K, the alloy showed an extraordinarily high strength of ~2.5 GPa combined with ~62%

in ductility. Serrated deformation, characterized by a sharp load drop and a temperature rise, can be seen beyond 21% strain. The amplitude of the load drop became increasingly larger with the deformation, approaching 570 MPa near the ultimate tensile strength. Note that this drop is even higher than the yield strength at room temperature and 140 K. The trend of load drop with deformation is shown in fig. S3. Figure 1C shows details of load drop and temperature rise in two consecutive serration events. The load drop was sharp, followed by a linear recovery over a time span of ~300 s. Continued loading triggers the next serration. It can be seen that the measured temperature started to increase after the stress dropped to the minimum value.

Figure 1D presents a plot of the strain-hardening rate at three temperatures. The initial rapid drop is attributed to dynamic recovery. As the temperature decreased, the HEA samples showed a higher and more stable strain hardening. The sample at 15 K exhibited the highest strain-hardening rate after the initial recovery, followed by the sample at 140 K, and the lowest hardening rate was at 295 K. At large strains, the strain-hardening rate for the 295 K sample continued to decrease with the deformation, while for the 15 K sample, the strain-hardening rate was stable until fracture.

Figure 1E shows the fractured sample at 15 K, with the fracture in the form of a wedge at nearly 45°. There was no significant necking even after 62% true strain, as commonly observed in conventional ductile alloys. By contrast, at 15 K, the ductile HEA sample was fractured by two shear bands at ~90° angles.

Lattice strain and texture evolution

The upper panels of Fig. 2 (A to C) show the evolution of lattice strains in LD at room temperature, 140 and 15 K, respectively. The lattice strain evolution for fcc HEAs at room temperature has been
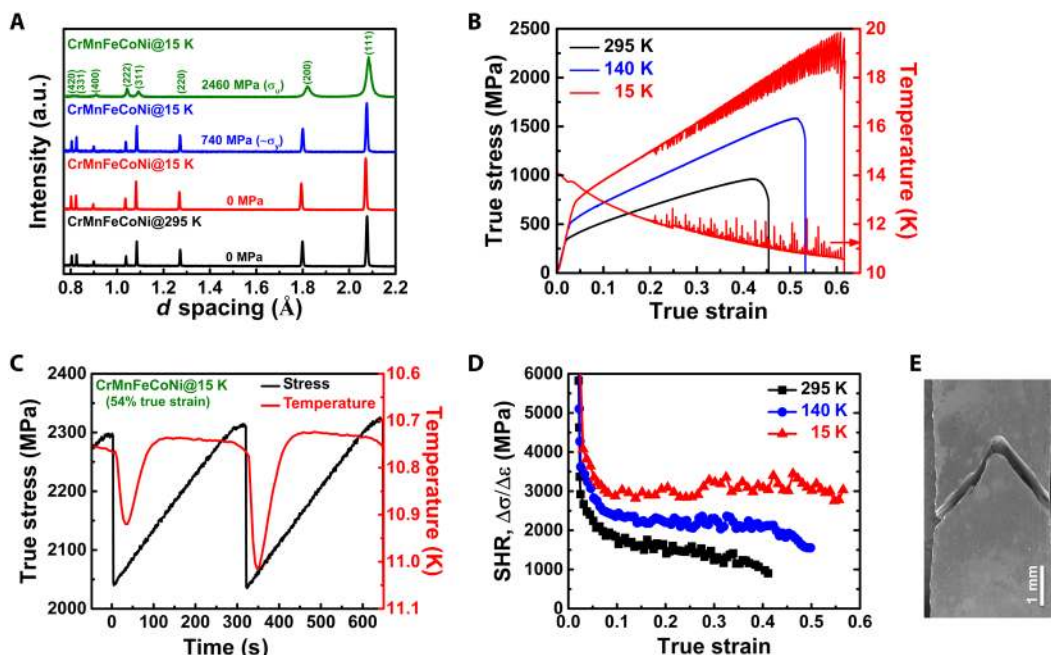
Fig. 1. Crystal structure and deformation behavior of CrMnFeCoNi alloy at low temperatures. (**A**) Selected diffraction patterns at room temperature and at 15 K during deformation, showing a clean single-phase fcc structure. (**B**) True stress-strain curves at room temperature, 140 K, and 15 K. The trend of temperature fluctuations (right-hand axis) due to serrations at 15 K is also superimposed. (**C**) Two serrations are shown with temperature (plotted in reverse scale for better comparison) to illustrate details of serrated deformation. (**D**) Plots of strain-hardening rate (SHR) at three temperatures. (**E**) Scanning electron microscopy image of the fractured sample at 15 K showing the 45° wedge.

Fig. 2. Lattice strain and texture development during deformation. Evolution of the lattice strain and the normalized integrated intensity for (*hkl*)//LD grains at (**A**) room temperature, (**B**) 140 K, and (**C**) 15 K for CrMnFeCoNi alloy. Below room temperature, the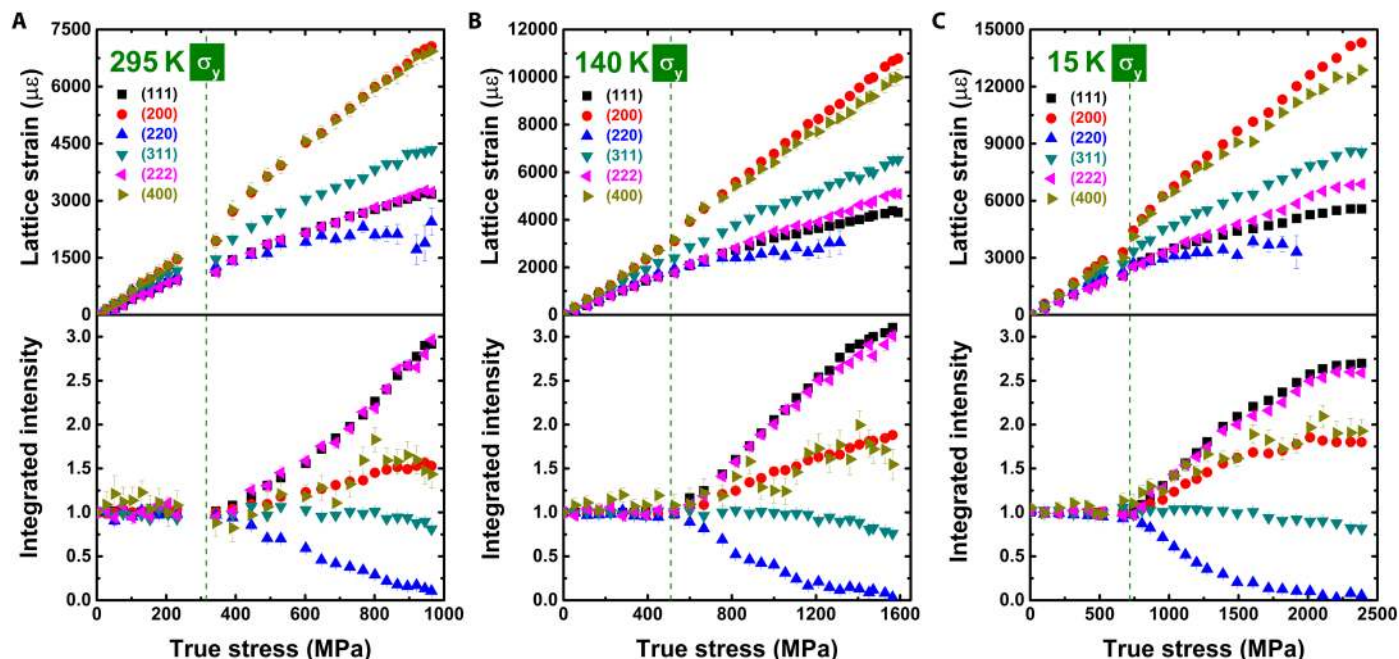 lattice strains for (111)//LD and (222)//LD split at large deformations. The same goes for (200)//LD and (400)//LD. The macroscopic yield strengths σ_y at different temperatures are indicated by vertical dashed lines.

well established (*16, 26*) and has many of the characteristics of that due to dislocation slip (*23, 24*). For fcc HEAs, (220) is the stiffest orientation and (220)//LD grains carry the highest load, causing (220)//LD grains to reach the yield strength faster than other grains. As a result, the (220) elastic lattice strain ceased to increase after yield. The yielding of the (220)//LD grains transferred the load to the more compliant orientation, e.g., (200)//LD, where large elastic strains developed.

Examination of the lattice strains measured with different orders of Miller indices yielded new information. At low temperatures, a split between ε_{111} and ε_{222} was observed (Fig. 2, B and C). In particular, $\varepsilon_{111} < \varepsilon_{222}$, and the gap widened at larger deformation strains. Similarly, a gap was also seen between (200) and (400) reflections, but with the opposite sign, i.e., $\varepsilon_{200} > \varepsilon_{400}$. The observed splits are signatures of deformation by stacking faults (SFs) (*27*).

The evolution of the integrated intensity for each reflection signifies the development of texture. The integrated intensity data, normalized by the initial stress-free values, are shown in the lower panels of Fig. 2 (A to C). In general, (111)//LD shows the largest increase in intensity, which means that the (111) grains are orientated toward the LD with increasing deformation. The intensity of (200)//LD also increased, but with a smaller magnitude, while the intensity of (220)//LD decreased. These experimental observations are signatures of the texture development due to dislocation slip in fcc metals and alloys (*23, 24*). At low temperatures, the texture developed slowly and plateaued due to the activation of additional deformation modes, which is discussed further below.

Deformation pathways at 15 K

Stacking fault probability (SFP), a measure of deformation faulting, is defined as the probability of finding a deformation fault between any two layers in the fcc stacking sequence (*27*). From the difference

between ε_{222} and ε_{111}, the SFP was calculated, following Warren (*27*). The evolution of SFP, together with the integrated intensity of (111)//LD in Fig. 3, provided insights into the transition of different deformation modes. As shown in Fig. 3, SFP is almost zero at room temperature. However, at 15 K, SFP developed early, when the stress > 1075 MPa, and increased to 27×10^{-3} before fracture.

The lower panel of Fig. 3 compares the texture development for (111)//LD at room temperature and 15 K. As indicated earlier, the texture development is characteristic of dislocation slip, so the (111)//LD texture was used as a measure of the dislocation activity. After yielding, the (111) intensity exhibits a sharp increase at room temperature. At 15 K, the (111) intensity also increases but at a slower pace. At large deformations, three distinct regions can be identified from the slope of the intensity curve. The vertical dashed lines in Fig. 3 show the critical points where different deformation modes kick in. The sample yielded at $\sigma \sim 718$ MPa ($\sigma_{y,15K}$), which can be seen from the increase in the (111)//LD texture. At $\sigma \sim 1075$ MPa, SFs started; before this point, the deformation was mainly by dislocations. The transition of dislocation slip to SF activity suggests that the generation of full dislocations is replaced by Shockley partials (*28*). At $\sigma \sim 1270$ MPa, the texture development slows down, but the SFP started to increase rapidly; this is also where serrations began (after a true strain of ~21%; see Fig. 1B). Thus, it appears that the serrated deformation coincided with the rapid development of SFs and a slowing down in dislocation activity. The last point of interest is at $\sigma \sim 2000$ MPa, where the (111) intensity reached a plateau, a sign of saturation of dislocations and the deformation proceeding mainly by SFs and twinning. This is also the point where massive serrations started with a load drop exceeding 200 MPa (fig. S3).

TEM images were collected on fractured samples and are shown in Fig. 4 to corroborate the findings by neutron diffraction. From Fig. 4A, the primary deformation mechanism in CrMnFeCoNi alloy
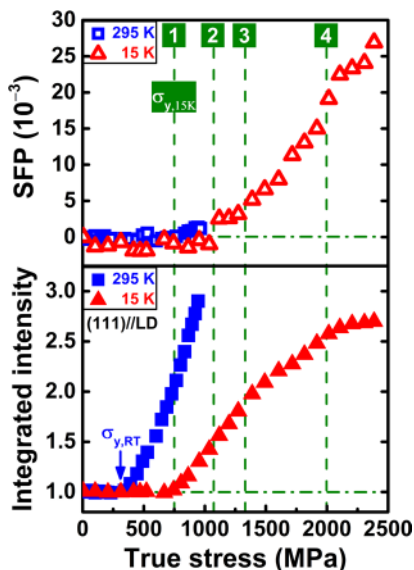
Fig. 3. Deformation pathway of CrMnFeCoNi HEA at 15 K. SFP and normalized integrated intensity of (111)//LD as a function of true stress are compared for room temperature and 15 K. Vertical dashed lines are drawn to pinpoint the changes in deformation behaviors in the 15 K dataset: (1) macroscopic yield point at $\sigma_{y,15K}$ ~ 718 MPa; (2) start of SFs (σ ~ 1075 MPa); (3) first sign of serration (σ ~ 1270 MPa), followed by a rapid increase in SFP and change in the slope of texture development; and (4) massive serrations coincided with the saturation of texture (σ ~ 2000 MPa).

at room temperature is the dislocation slip. Sparse twins were also observed in some regions (Fig. 4B), which is a direct result of the relatively high stacking fault energy (SFE) at room temperature (*29*, *30*). For the sample at 15 K, SFs were widely observed (Fig. 4C) and a very high density of twins is also evident from Fig. 4D. These observations, along with the high SFP obtained by neutron diffraction, indicate that the SFE decreased appreciably on cooling to 15 K. In addition, the formation of intersecting twins was observed, which resulted in a twinning network due to the activation of multiple twinning systems (Fig. 4E). The selected-area diffraction (SAD) pattern is presented as an inset of Fig. 4E, where the additional bright spots demonstrated clear evidence of twinning. The high-resolution TEM (HR-TEM) image in Fig. 4F also shows twins at 15 K.

Deformation diagram for fcc HEAs

While the low-temperature deformation behaviors are illustrated in detail with a quinary CrMnFeCoNi alloy, similar deformation behaviors were also observed in quaternary CrFeCoNi and ternary CrCoNi alloys. Taking these data together, a deformation diagram (Fig. 5) was constructed on the basis of the activation strains for SF and serration. The critical strain for SF activation in Fig. 5 shows a systematic decrease with decreasing temperature, demonstrating the lowering of SFE on cooling. When compared to the quinary alloy, the entire curve of SF activation for CrFeCoNi shifted downward, a manifestation of the composition dependence of the SFE. The trend continued for the ternary CrCoNi, where the SFs started at lower strain values. For the activation strain for serration, the values for the quinary and quaternary alloys are close to each other, while in the ternary alloy the serration starts early, at ~11% strain.

DISCUSSION

It is intriguing that HEAs exhibit extreme work hardening, while other alloys suffer from reduced ductility at ultralow temperatures. We believe that this is related to the chemistry and structure of HEAs. The fcc structure facilitates slip, so plastic deformation can easily start with dislocations. However, in contrast to conventional fcc alloys, the crystal lattice of HEAs is distorted due to the presence of multicomponents, which renders the magnitude of Burgers vector ill defined with segmented wiggled dislocation lines and offers resistance against dislocation motion (*31*). As a result, the propagation of dislocations is hindered, and this has led to the multiplication and hence high density of dislocations. Room temperature study shows that the dislocation density is already reaching ~10^{15} m^{-2} level (*16*), which could be even higher when the temperature is lowered.

Because of the favorable composition, the SFE in these HEAs is low (*29*, *30*, *32*), thereby allowing a transition from deformation by full dislocations to partials with SFs and twinning (*28*, *33*). As the neutron diffraction data demonstrated, the critical strain for SF decreases nearly linearly with temperature. Thus, at ultralow temperatures, SF becomes a competitive deformation mode, with a high probability of SFs. Continuing deformation led to cross-slip and cross-twinning, ultimately causing plastic instability and hence the serration. Normally, serrations at low temperatures limit the ductility (*20*, *21*). It is thus remarkable that the ductility of HEAs continued to increase in the presence of serrations. It is likely that in HEAs, the local disorder (e.g., stress field caused by size mismatch) (*34*) resulting from the multicomponent nature of HEAs successfully prevented the propagation of serration flow, thus leading to continued strengthening until major shear bands form fracturing the sample.

Quantitative analysis of the experimental data suggests that SFs played a critical role bridging dislocation slip and serration. Without SFs, the alloys would have gone from dislocation slip straight to serrations and would fail early with a reduced ductility, like other alloys at low temperature. Deformation by SF was made possible by two factors.

(i) The alloys remained in the fcc phase at 15 K, as the neutron diffraction data demonstrated for all samples. This was a surprising finding because the first-principle calculations predicted a stable hcp phase at low temperatures for a solid solution with a random distribution of constituent elements (*19*, *35*). One possible explanation is that, as a recent theoretical study suggested, the SFE varies widely depending on the short-range chemical order and can even become positive depending on the local configurations (*36*). Another possibility, as Ma *et al.* (*35*) argued, is that the fcc phase may be stabilized by kinetics at low temperatures.

(ii) The SFE is sufficiently low so that SFs can start at an immediate step before serrations. The experimental values of SFE at room temperature for CrMnFeCoNi, CrFeCoNi, and CrCoNi are 30 ± 5 mJ/m^2 (*29*), 27 ± 4 mJ/m^2 (*32*), and 22 ± 4 mJ/m^2 (*30*), respectively. These values can be compared with the SFE of Ni (the only fcc element in these alloys), which is 125 ± 5 mJ/m^2 (*37*). At low temperatures, the SFEs were further suppressed, as is evident from the early activation of SFs at 140 and 15 K. Recent studies by first-principle calculations suggested that the temperature dependence of SFE is strongly linked to the entropy terms, including configurational entropy, vibrational entropy, and magnetic entropy (*35*, *38*). Among these entropy contributions, the vibrational entropy due to high-frequency phonon modes has been highlighted as a term dominating the temperature dependence (*38*).
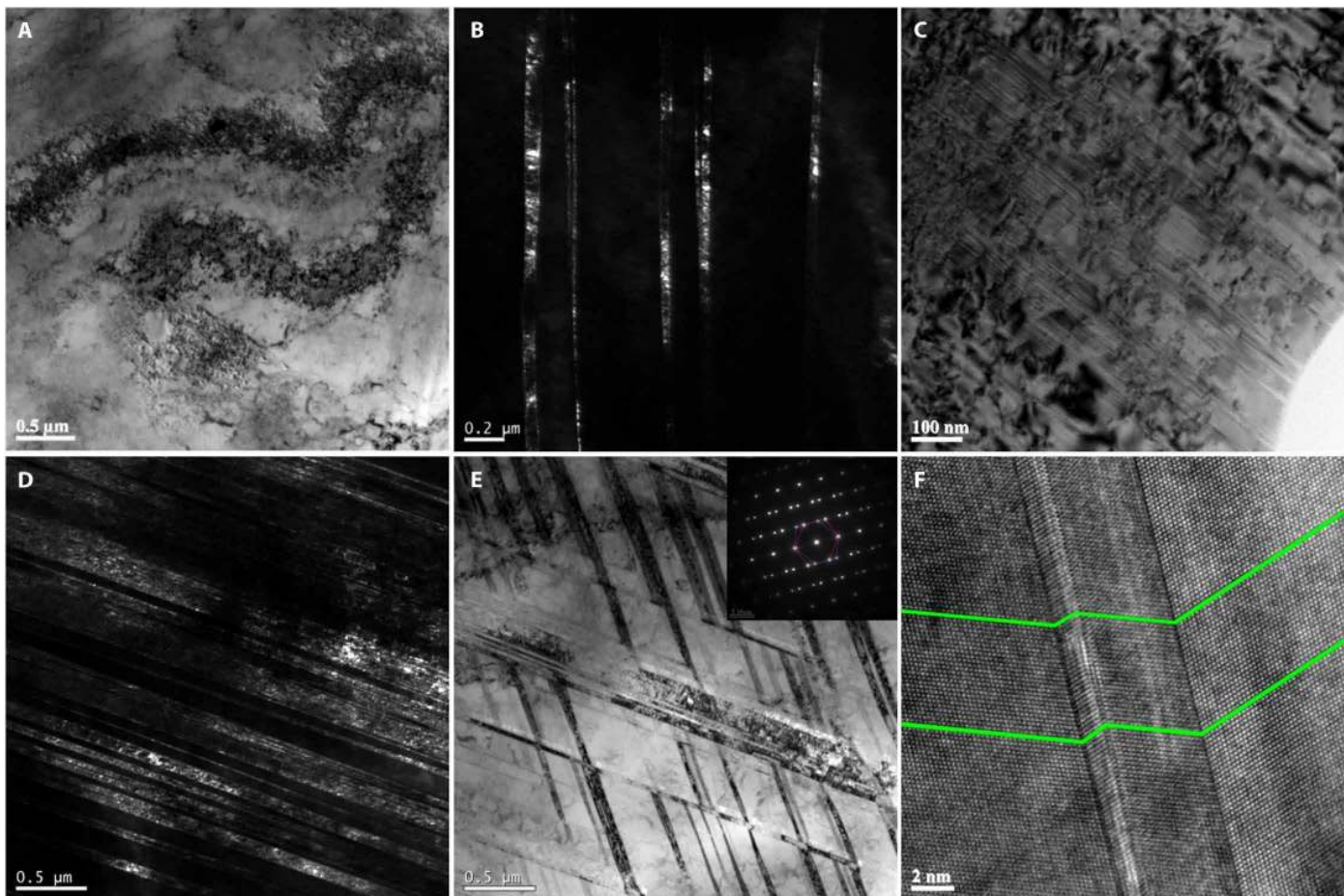
Fig. 4. Electron microscopy results of fractured samples. TEM images at room temperature showing the dislocation pileups (**A**), while the dark-field image also shows some sparse twins (**B**). The 15 K sample has a large number of SFs (**C**) and a very high density of closely spaced twins (**D**). An intersecting twinning network is formed at 15 K (**E**), while the SAD pattern in the inset shows the additional bright spots due to twinning. (**F**) HR-TEM taken from the 15 K sample shows deformation twins, with the twin boundaries marked.

The observed SFs, twinning, and serrations at 15 K are the source of the increased strain-hardening rate at low temperatures. At room temperature, the deformation is dominated by dislocation activities, which gives rise to a characteristic strain-hardening rate. At low temperature, dislocation activities are still important, as the deformation starts with dislocation slip, but the role of additional deformation modes is also evident from the strain-hardening rate curves in Fig. 1D, where a higher and stable hardening rate was observed, especially for the sample at 15 K. The additional deformation mechanisms resulted in minimum necking (Fig. 1E) and hence more significant uniform elongation and higher strength.

As the in situ data in Fig. 3 demonstrated, deformation at 15 K started with dislocation slip. SFs and twinning became active later. This observation provided important clues regarding the microscopic origin of the increased work hardening at 15 K. It has been predicted by first-principle calculations that, for the HEAs studied here, the stable phase is hcp (*19, 38, 39*). An fcc to hcp phase transition has been reported in CrMnFeCoNi under pressure, demonstrating the metastable nature of the fcc phase at room temperature (*40*). The fcc phase, a stable phase at high temperature, becomes increasingly unstable as the temperature approaches absolute zero. It is important

to note that the pathway from fcc to hcp is through SFs, as the hcp phase is formed by changing the stacking sequence from A-B-C-A-B-C in fcc to A-B-A-B in hcp (*28*). While the fcc phase starts to deform by dislocation slip, SFs are activated at large strains when the fcc becomes unstable. Deformation by SFs, and subsequently twinning, creates an additional boundary. It has been shown by Zhu *et al.* (*41*) that there are significant energy barriers for a dislocation to cross the SF or twin boundary. The additional stress to overcome the barrier, due to the interaction between dislocations and SFs and twin boundaries, impedes the propagation of dislocations and gives rise to the extreme work hardening, leading to the unusually large ductility at 15 K. To this end, the in situ neutron diffraction experiments underscored the underlying link between the preferred deformation mechanism and lattice instability.

Recently, Sun *et al.* (*42*) conducted an ex situ TEM study on ultrafine-grained CrMnFeCoNi HEA at 77 K, where HR-TEM images showed deformation twins and some evidence of SFs. Our in situ experiments at 15 K, a lower temperature, demonstrated that SFs became abundant and an additional deformation mechanism, serration, emerged. Unlike dislocations, SFs, and twinning that occur across the entire test specimen, serration is a form of inhomogeneous
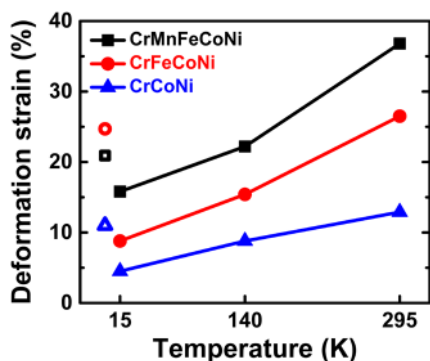
Fig. 5. Deformation diagram of fcc HEAs. The critical strain at which the SFs and serrated deformation were activated. In quinary CrMnFeCoNi, the SFs are observed only at a strain value closer to fracture (36.8% in true strain) at 295 K, while at low temperatures, the SFs appear earlier, after ~22.2% at 140 K and ~15.8% at 15 K, respectively. The SFs form more easily in the quaternary CrFeCoNi alloy, where the SFs start at lower deformation strains for all three temperatures. The trend continues for the ternary CrCoNi alloy, where SFs begin to form even at an early stage of deformation at room temperature. The open symbols are the activation strain for serrations at 15 K (the data points are displaced to the left-hand side for clarity), which are substantially higher than the critical strains for SFs.

deformation localized in particular regions. Serrations are commonly observed in metallic glasses, where other deformation mechanisms associated with crystalline materials are not available (43). Serration behavior has also been reported in Al-containing HEAs (3, 44). However, the serration events in Al-containing HEAs occur at high temperatures, which is qualitatively different from our observations at 15 K. High-temperature serrations are associated with dynamic strain aging, arising from the interaction between diffusing solutes (in this case, Al atoms) and dislocations (44). The magnitude of the load drop for serration at high temperatures, also known as the Portevin–Le Chatelier (PLC) effect, is extremely small compared to that observed for HEAs at 15 K. At ultralow temperatures, where the diffusion is frozen, the serration occurs through different mechanisms (20, 21).

There are presently two schools of thought regarding the mechanism of serration at low temperatures: (i) mechanical origin due to the instability of plastic deformation (e.g., dislocation pileups) or (ii) a manifestation of thermodynamic instability where the specific heat and thermal conductivity vanish (20, 21, 45). In our experiments, as can be seen from Fig. 1C, the temperature rise follows the load drop, suggesting that the temperature rise is a consequence of the load drop. However, it is cautioned that, in this experiment, the thermocouples were located at the sample grips, not on the sample. Thus, there could be a delay in the temperature sensor. For the same reason, the local temperature rise in the deformed region could also be much higher. It is possible then that locally, the HEAs were heated to a very high temperature state by the adiabatic heat release, where some of the deformation was annealed during the recovery (~50 s from the temperature data), before the region of serration was cooled back to ~15 K.

In summary, in situ neutron diffraction measurements revealed that the extreme work hardening observed in HEAs at 15 K is the result of the cooperation of multiple deformation mechanisms at low temperatures. Like at room temperature, the deformation at 15 K started with dislocation slip, but SFs and twinning were activated

at larger strains before transitioning to serrations. The activation of these additional deformation mechanisms is the source of the extreme work hardening and the exceedingly large ductility observed at 15 K. The intermediate step, SF, is critically important and highlights the influence of entropy and lattice instability on deformation and mechanical behaviors. As our study shows, the unique combination of complex chemistry and simple crystal structure may hold the key to the design of new materials for applications at low temperatures, where the competitive mechanisms can be deployed in synergy to produce materials with high strength and superior ductility.

MATERIALS AND METHODS
Sample preparation
Ingots of $Cr_{20}Mn_{20}Fe_{20}Co_{20}Ni_{20}$, $Cr_{25}Fe_{25}Co_{25}Ni_{25}$, and $Cr_{33.3}Co_{33.3}Ni_{33.3}$ (atomic %) alloys were fabricated by arc melting a mixture of pure elements (purity > 99.9%) in a Ti-gettered high-purity argon atmosphere. To ensure composition homogeneity, the ingots were flipped over and remelted eight times. Last, they were drop-cast into rectangular Cu-mold of dimensions 15 mm × 15 mm × 65 mm. The ingots were homogenized by annealing at 1200°C for 24 hours under inert argon atmosphere followed by quenching in iced water. Cold rolling was conducted to ~80% reduction in thickness (15 to ~3.1 mm) to break down the dendritic structure, followed by recrystallization treatment at 800°C for 1 hour and iced-water quenching. The equiaxed grains were obtained with an average grain size of ~5 μm. Rectangular dog-bone shaped tensile specimens with gauge dimensions of 3 mm × 4 mm × 25 mm (thickness × width × length) were prepared by electrical discharge machining.

In situ neutron diffraction measurements
The in situ neutron diffraction experiments under tensile loading were conducted at the Engineering Materials Diffractometer TAKUMI (beamline 19) at the Materials and Life Science Experimental Facility (MLF) of Japan Proton Accelerator Research Complex (J-PARC) using a cryogenic load frame. The sample, 45° to the incident neutron beam, was mounted inside the cryogenic loading cell chamber, which was sealed and evacuated to <10^{-3} kPa before the cooling was started. A Gifford-McMahon (GM) cooler installed in the cryogenic load frame was used to cool the grips and the specimen. The GM cooler had two stages of 50 and 4.2 K, respectively. The 4.2 K stage wound with a heater wire was connected to both grips using copper wires. The calibrated Cernox thermosensors were mounted on the Cu-Be grips to monitor and control the temperature. The details of this cryogenic load frame for the neutron diffractometer have been reported in (46). To monitor the sample temperature, we attached two thermocouples on both sides of sample mount. Note that the thermocouple could not be fixed on the sample gauge section to avoid the incident neutron beam. The sample was cooled down and held for ~1 hour at a stable temperature of 15 K (vacuum ~ 10^{-5} kPa) before the loading was commenced. Samples were loaded in 10 equal steps in the elastic region and held for 10 min at each step to obtain good statistics. Continuous loading was carried out in the plastic regime at a strain rate of 0.04 mm/min (2.67×10^{-5} s^{-1}). The time-of-flight (TOF) neutron diffraction data were acquired simultaneously for the loading and transverse directions by two detector banks, at ±90° to the incident neutron beam. The data at 140 K and room temperature were also obtained in a similar manner.

Data analysis

Rietveld refinement for multiple peak fitting of the neutron diffraction data was carried out using Z-Rietveld software (*47*). Lattice strain ε_{hkl} was calculated from the TOF data by the following method

$$\varepsilon_{hkl} = \frac{(d_{hkl} - \mathring{d}_{hkl})}{\mathring{d}_{hkl}} = \frac{(\mathrm{TOF}_{hkl} - \mathrm{TOF}^{\circ}_{hkl})}{\mathrm{TOF}^{\circ}_{hkl}}$$

where d_{hkl} is the lattice spacing of *hkl* planes, $\mathring{d}_{hkl}$ is the value for the stress-free sample, and TOF_{hkl} is the Bragg position of the *hkl* reflection in the TOF data.

SFP was calculated from the lattice strain by following equation 13.67 provided by Warren (*27*)

$$\varepsilon_{hkl} = \frac{-\sqrt{3}\,\alpha}{4\pi\,h_o^2(u+b)}\sum_b(\pm)\,L_o$$

where ε_{hkl} is the experimentally measured lattice strain for the specific *hkl* reflection, α is the SFP, $h_o^2 = h^2 + k^2 + l^2$ for the cubic system, $(u + b)$ represents the total number of unbroadened and broadened components, $L_o = 3N \pm 1$ for components broadened by faulting, and $L_o = 3N$ for components not broadened by faulting. To calculate SFP from the lattice strain of (111) and (222), a simplified equation was obtained by inputting the $\frac{1}{h_o^2(u+b)}\sum_b(\pm)\,L_o$ value of $+\frac{1}{4}$ for (111) reflection and $-\frac{1}{8}$ for (222) reflection (*27*). It follows

$$\mathrm{SFP} = \frac{32\pi}{3\sqrt{3}}(\varepsilon_{222} - \varepsilon_{111})$$

where ε_{222} and ε_{111} are the experimentally measured lattice strain values with applied stress for (222) and (111) reflections, respectively. Adjacent reflections were used from the lattice strain plots for the SFP calculation, as their difference due to faulting can be observed for the in situ neutron diffraction deformation data (Fig. 2). The measured lattice strain for (111) and (222) reflections should be the same as they are crystallographically equivalent. However, SFs led to the difference in their lattice strain due to deformation faulting (*27*). The SFP behavior was also verified from the (200) and (400) pair [$\mathrm{SFP} = -\frac{16\pi}{3\sqrt{3}}(\varepsilon_{400} - \varepsilon_{200})$]; the effect was opposite as illustrated in Fig. 2 (B and C).

Transmission electron microscopy

For microstructural examination of fractured samples, a Tecnai F30 TEM operated at 300 kV acceleration voltage was used. TEM specimens with a diameter of 3 mm were cut from the deformed samples and then ground to around 50 μm by 2000-grit SiC paper under the press of a rubber plug, followed by twin-jet electropolishing using a mixed solution of $HClO_4$:C_2H_6O (volume ratio, 1:9) with a direct voltage of 30 V and a current of 50 mA at a temperature of 243 K.

SUPPLEMENTARY MATERIALS

Supplementary material for this article is available at http://advances.sciencemag.org/cgi/content/full/6/13/eaax4002/DC1

Fig. S1. Lattice parameter change during cooling.
Fig. S2. Structure evolution of CrMnFeCoNi HEA with time.
Fig. S3. The magnitude of load drops with deformation.

REFERENCES AND NOTES

1. A. Suzuki, H. Inui, T. M. Pollock, L1₂-strengthened cobalt-base superalloys. *Annu. Rev. Mater. Res.* **45**, 345–368 (2015).
2. P. Gumbsch, J. Riedle, A. Hartmaier, H. F. Fischmeister, Controlling factors for the brittle-to-ductile transition in tungsten single crystals. *Science* **282**, 1293–1295 (1998).
3. Y. Zhang, T. T. Zuo, Z. Tang, M. C. Gao, K. A. Dahmen, P. K. Liaw, Z. P. Lu, Microstructures and properties of high-entropy alloys. *Prog. Mater. Sci.* **61**, 1–93 (2014).
4. B. Gludovatz, A. Hohenwarter, D. Catoor, E. H. Chang, E. P. George, R. O. Ritchie, A fracture-resistant high-entropy alloy for cryogenic applications. *Science* **345**, 1153–1158 (2014).
5. Z. Li, K. G. Pradeep, Y. Deng, D. Raabe, C. C. Tasan, Metastable high-entropy dual-phase alloys overcome the strength–ductility trade-off. *Nature* **534**, 227–230 (2016).
6. Z. J. Zhang, M. M. Mao, J. Wang, B. Gludovatz, Z. Zhang, S. X. Mao, E. P. George, Q. Yu, R. O. Ritchie, Nanoscale origins of the damage tolerance of the high-entropy alloy CrMnFeCoNi. *Nat. Commun.* **6**, 10143 (2015).
7. Z. Fu, L. Jiang, J. L. Wardini, B. E. MacDonald, H. Wen, W. Xiong, D. Zhang, Y. Zhou, T. J. Rupert, W. Chen, E. J. Lavernia, A high-entropy alloy with hierarchical nanoprecipitates and ultrahigh strength. *Sci. Adv.* **4**, eaat8712 (2018).
8. P. Shi, W. Ren, T. Zheng, Z. Ren, X. Hou, J. Peng, P. Hu, Y. Gao, Y. Zhong, P. K. Liaw, Enhanced strength–ductility synergy in ultrafine-grained eutectic high-entropy alloys by inheriting microstructural lamellae. *Nat. Commun.* **10**, 489 (2019).
9. H. Luo, W. Lu, X. Fang, D. Ponge, Z. Li, D. Raabe, Beating hydrogen with its own weapon: Nano-twin gradients enhance embrittlement resistance of a high-entropy alloy. *Mater. Today* **21**, 1003–1009 (2018).
10. F. Granberg, K. Nordlund, M. W. Ullah, K. Jin, C. Lu, H. Bei, L. M. Wang, F. Djurabekova, W. J. Weber, Y. Zhang, Mechanism of radiation damage reduction in equiatomic multicomponent single phase alloys. *Phys. Rev. Lett.* **116**, 135504 (2016).
11. N. A. P. K. Kumar, C. Li, K. J. Leonard, H. Bei, S. J. Zinkle, Microstructural stability and mechanical behavior of FeNiMnCr high entropy alloy under ion irradiation. *Acta Mater.* **113**, 230–244 (2016).
12. O. N. Senkov, G. B. Wilks, J. M. Scott, D. B. Miracle, Mechanical properties of Nb₂₅Mo₂₅Ta₂₅W₂₅ and V₂₀Nb₂₀Mo₂₀Ta₂₀W₂₀ refractory high entropy alloys. *Intermetallics* **19**, 698–706 (2011).
13. C. Lee, G. Song, M. C. Gao, R. Feng, P. Chen, J. Brechtl, Y. Chen, K. An, W. Guo, J. D. Poplawsky, S. Li, A. T. Samaei, W. Chen, A. Hu, H. Choo, P. K. Liaw, Lattice distortion in a strong and ductile refractory high-entropy alloy. *Acta Mater.* **160**, 158–172 (2018).
14. P. Koželj, S. Vrtnik, A. Jelen, S. Jazbec, Z. Jagličić, S. Maiti, M. Feuerbacher, W. Steurer, J. Dolinšek, Discovery of a superconducting high-entropy alloy. *Phys. Rev. Lett.* **113**, 107001 (2014).
15. G. Laplanche, A. Kostka, O. M. Horst, G. Eggeler, E. P. George, Microstructure evolution and critical stress for twinning in the CrMnFeCoNi high-entropy alloy. *Acta Mater.* **118**, 152–163 (2016).
16. B. Wang, H. He, M. Naeem, S. Lan, S. Harjo, T. Kawasaki, Y. Nie, H. W. Kui, T. Ungár, D. Ma, A. D. Stoica, Q. Li, Y. Ke, C. T. Liu, X.-L. Wang, Deformation of CoCrFeNi high entropy alloy at large strain. *Scr. Mater.* **155**, 54–57 (2018).
17. W. Woo, E.-W. Huang, J.-W. Yeh, H. Choo, C. Lee, S.-Y. Tu, In-situ neutron diffraction studies on high-temperature deformation behavior in a CoCrFeMnNi high entropy alloy. *Intermetallics* **62**, 1–6 (2015).
18. O. Grässel, L. Krüger, G. Frommeyer, L. W. Meyer, High strength Fe–Mn–(Al, Si) TRIP/TWIP steels development—Properties—Application. *Int. J. Plast.* **16**, 1391–1409 (2000).
19. S. Huang, W. Li, S. Lu, F. Tian, J. Shen, E. Holmström, L. Vitos, Temperature dependent stacking fault energy of FeCrCoNiMn high entropy alloy. *Scr. Mater.* **108**, 44–47 (2015).
20. D. A. Wigley, *Mechanical Properties of Materials at Low Temperatures* (Plenum Press, 1971).
21. V. V. Pustovalov, Serrated deformation of metals and alloys at low temperatures (Review). *Low Temp. Phys.* **34**, 683–723 (2008).
22. D. B. Williams, C. B. Carter, *Transmission Electron Microscopy* (Springer, ed. 2, 2009).
23. B. Clausen, T. Lorentzen, T. Leffers, Self-consistent modelling of the plastic deformation of f.c.c. polycrystals and its implications for diffraction measurements of internal stresses. *Acta Mater.* **46**, 3087–3098 (1998).
24. S. Cheng, A. D. Stoica, X.-L. Wang, Y. Ren, J. Almer, J. A. Horton, C. T. Liu, B. Clausen, D. W. Brown, P. K. Liaw, L. Zuo, Deformation crossover: From nano- to mesoscale. *Phys. Rev. Lett.* **103**, 035502 (2009).
25. S. Harjo, K. Aizawa, T. Kowasaki, T. Nakamoto, T. Hemmi, T. Iwahashi, Cryogenic loading devices for materials science and engineering studies at J-PARC. *JAEA Conf.* **48**, 441–447 (2016).
26. Y. Wu, W. H. Liu, X.-L. Wang, D. Ma, A. D. Stoica, T. G. Nieh, Z. B. He, Z. P. Lu, In-situ neutron diffraction study of deformation behavior of a multi-component high-entropy alloy. *Appl. Phys. Lett.* **104**, 051910 (2014).
27. B. E. Warren, *X-ray Diffraction* (Dover Publications, 1990).
28. D. Hull, D. J. Bacon, *Introduction to Dislocations* (Butterworth-Heinemann, ed. 5, 2011).
29. N. L. Okamoto, S. Fujimoto, Y. Kambara, M. Kawamura, Z. M. T. Chen, H. Matsunoshita, K. Tanaka, H. Inui, E. P. George, Size effect, critical resolved shear stress, stacking fault

energy, and solid solution strengthening in the CrMnFeCoNi high-entropy alloy. *Sci. Rep.* **6**, 35863 (2016).

30. G. Laplanche, A. Kostka, C. Reinhart, J. Hunfeld, G. Eggeler, E. P. George, Reasons for the superior mechanical properties of medium-entropy CrCoNi compared to high-entropy CrMnFeCoNi. *Acta Mater.* **128**, 292–303 (2017).

31. Y. Y. Zhao, T. G. Nieh, Correlation between lattice distortion and friction stress in Ni-based equiatomic alloys. *Intermetallics* **86**, 45–50 (2017).

32. S. F. Liu, Y. Wu, H. T. Wang, J. Y. He, J. B. Liu, C. X. Chen, X. J. Liu, H. Wang, Z. P. Lu, Stacking fault energy of face-centered-cubic high entropy alloys. *Intermetallics* **93**, 269–273 (2018).

33. C. Niu, C. R. LaRosa, J. Miao, M. J. Mills, M. Ghazisaeidi, Magnetically-driven phase transformation strengthening in high entropy alloys. *Nat. Commun.* **9**, 1363 (2018).

34. F. Zhang, Y. Tong, K. Jin, H. Bei, W. J. Weber, A. Huq, A. Lanzirotti, M. Newville, D. C. Pagan, J. Y. P. Ko, Y. Zhang, Chemical complexity induced local structural distortion in NiCoFeMnCr high-entropy alloy. *Mater. Res. Lett.* **6**, 450–455 (2018).

35. D. Ma, B. Grabowski, F. Körmann, J. Neugebauer, D. Raabe, Ab initio thermodynamics of the CoCrFeMnNi high entropy alloy: Importance of entropy contributions beyond the configurational one. *Acta Mater.* **100**, 90–97 (2015).

36. J. Ding, Q. Yu, M. Asta, R. O. Ritchie, Tunable stacking fault energies by tailoring local chemical order in CrCoNi medium-entropy alloys. *Proc. Natl. Acad. Sci. U.S.A.* **115**, 8919–8924 (2018).

37. C. B. Carter, S. M. Holmes, The stacking-fault energy of nickel. *Philos. Mag.* **35**, 1161–1171 (1977).

38. S. Zhao, G. M. Stocks, Y. Zhang, Stacking fault energies of face-centered cubic concentrated solid solution alloys. *Acta Mater.* **134**, 334–345 (2017).

39. Y. H. Zhang, Y. Zhuang, A. Hu, J. J. Kai, C. T. Liu, The origin of negative stacking fault energies and nano-twin formation in face-centered cubic high entropy alloys. *Scr. Mater.* **130**, 96–99 (2017).

40. F. Zhang, Y. Wu, H. Lou, Z. Zeng, V. B. Prakapenka, E. Greenberg, Y. Ren, J. Yan, J. S. Okasinski, X. Liu, Y. Liu, Q. Zeng, Z. Lu, Polymorphism in a high-entropy alloy. *Nat. Commun.* **8**, 15687 (2017).

41. Y. T. Zhu, X. L. Wu, X. Z. Liao, J. Narayan, L. J. Kecskés, S. N. Mathaudhu, Dislocation–Twin interactions in nanocrystalline fcc metals. *Acta Mater.* **59**, 812–821 (2011).

42. S. J. Sun, Y. Z. Tian, X. H. An, H. R. Lin, J. W. Wang, Z. F. Zhang, Ultrahigh cryogenic strength and exceptional ductility in ultrafine-grained CoCrFeMnNi high-entropy alloy with fully recrystallized structure. *Mater. Today Nano* **4**, 46–53 (2018).

43. C. A. Schuh, T. G. Nieh, A nanoindentation study of serrated flow in bulk metallic glasses. *Acta Mater.* **51**, 87–99 (2003).

44. J. Brechtl, S. Y. Chen, X. Xie, Y. Ren, J. W. Qiao, P. K. Liaw, S. J. Zinkle, Towards a greater understanding of serrated flows in an Al-containing high-entropy-based alloy. *Int. J. Plast.* **115**, 71–92 (2019).

45. Z. S. Basinski, The instability of plastic flow of metals at very low temperatures. *Proc. R. Soc. Lond. A Math. Phys. Sci.* **240**, 229–242 (1957).

46. X. Jin, T. Nakamoto, S. Harjo, T. Hemmi, T. Umeno, T. Ogitsu, A. Yamamoto, M. Sugano, K. Aizawa, J. Abe, W. Gong, T. Iwahashi, Development of a cryogenic load frame for the neutron diffractometer at Takumi in Japan Proton Accelerator Research Complex. *Rev. Sci. Instrum.* **84**, 063106 (2013).

47. R. Oishi-Tomiyasu, M. Yonemura, T. Morishima, A. Hoshikawa, S. Torii, T. Ishigaki, T. Kamiyama, Application of matrix decomposition algorithms for singular matrices to the Pawley method in Z-Rietveld. *J. Appl. Cryst.* **45**, 299–308 (2012).

Science Advances

Cooperative deformation in high-entropy alloys at ultralow temperatures

Muhammad Naeem, Haiyan He, Fan Zhang, Hailong Huang, Stefanus Harjo, Takuro Kawasaki, Bing Wang, Si Lan, Zhenduo Wu, Feng Wang, Yuan Wu, Zhaoping Lu, Zhongwu Zhang, Chain T. Liu and Xun-Li Wang

ARTICLE TOOLS	http://advances.sciencemag.org/content/6/13/eaax4002
SUPPLEMENTARY MATERIALS	http://advances.sciencemag.org/content/suppl/2020/03/23/6.13.eaax4002.DC1
REFERENCES	This article cites 43 articles, 4 of which you can access for free http://advances.sciencemag.org/content/6/13/eaax4002#BIBL
PERMISSIONS	http://www.sciencemag.org/help/reprints-and-permissions

Use of this article is subject to the Terms of Service